RESEARCH: Original Research

ELSEVIER

Strong interlayer coupling and long-lived interlayer excitons in two-dimensional perovskite derivatives and transition metal dichalcogenides van der Waals heterostructures

Jia Liang [a,b,1], Qing Ai [a,1], Xiewen Wen [c,d,1], Xiuyu Tang [e], Tianshu Zhai [a], Rui Xu [a], Xiang Zhang [a], Qiyi Fang [a], Christine Nguyen [a], Yifeng Liu [a], Hanyu Zhu [a], Tanguy Terlier [h], Gary P. Wiederrecht [c], Pulickel M. Ajayan [a], Xiaofeng Qian [e,f,g,*], Jun Lou [a,*]

[a] Department of Materials Science and NanoEngineering, Rice University, Houston, TX, USA
[b] Department of Materials Science, Fudan University, Shanghai, China
[c] Center for Nanoscale Materials, Argonne National Laboratory, Lemont, IL, USA
[d] Department of ISE, University Research Facility in 3D Printing, and State Key Laboratory of Ultra-precision Machining Technology, The Hong Kong Polytechnic University, Hong Kong, China
[e] Department of Materials Science and Engineering, Texas A&M University, College Station, TX, USA
[f] Department of Physics and Astronomy, Texas A&M University, College Station, TX, USA
[g] Department of Electrical and Computer Engineering, Texas A&M University, College Station, TX, USA
[h] Shared Equipment Authority, SIMS Laboratory, Rice University, Houston, TX, USA

Two-dimensional (2D) van der Waals (vdW) heterostructures offer new platforms for exploring novel physics and diverse applications ranging from electronics and photonics to optoelectronics at the nanoscale. The studies to date have largely focused on transition-metal dichalcogenides (TMDCs) based samples prepared by mechanical exfoliation method, therefore it is of significant interests to study high-quality vdW heterostructures using novel materials prepared by a versatile method. Here, we report a two-step vapor phase growth process for the creation of high-quality vdW heterostructures based on perovskites and TMDCs, such as 2D $Cs_3Bi_2I_9$/$MoSe_2$, with a large lattice mismatch. Supported by experimental and theoretical investigations, we discover that the $Cs_3Bi_2I_9$/$MoSe_2$ vdW heterostructure possesses hybrid band alignments consisting of type-I and type-II heterojunctions because of the existence of defect energy levels in $Cs_3Bi_2I_9$. More importantly, we demonstrate that the type-II heterojunction in the $Cs_3Bi_2I_9$/$MoSe_2$ vdW heterostructure not only shows a higher interlayer exciton density, but also exhibits a longer interlayer exciton lifetime than traditional 2D TMDCs based type-II heterostructures. We attribute this phenomenon to the reduced overlap of electron and hole wavefunctions caused by the large lattice mismatch. Our work demonstrates that it is possible to directly grow high-quality vdW heterostructures based on entirely different materials which provide promising platforms for exploring novel physics and cutting-edge applications, such as optoelectronics, valleytronics, and high-temperature superfluidity.

---

* Corresponding authors at: Department of Materials Science and Engineering, Texas A&M University, College Station, TX, USA (Xiaofeng Qian); Department of Materials Science and NanoEngineering, Rice University, Houston, TX, USA (J. Lou).
E-mail addresses: Qian, X. (feng@tamu.edu), Lou, J. (jlou@rice.edu).
[1] These authors contributed equally to this work.

1

Introduction

Two-dimensional van der Waals (vdW) heterostructures have emerged as a family of materials for next-generation atomically thin electronics and optoelectronics because of their diverse functionalities [1–8]. Tremendous progress has been made in exploring the vdW heterostructures with long interlayer exciton lifetime in 2D TMDCs systems, such as $MoSe_2/WSe_2$, MoS_2/WSe_2, and MoS_2/WS_2 [9–18]. However, these vdW heterostructures have been mostly fabricated manually using mechanically exfoliated flakes, which oftentimes resulted in low-quality samples with a random domain size and contaminated interface. Additionally, current fabrication technique is time consuming and difficult to scale-up for practical industrial applications. In contrast, direct chemical vapor deposition (CVD) growth of vertical vdW heterostructures endows them well-defined interlayer orientations and clean interfaces. It should be noted that a few vdW heterostructures have already been prepared by the CVD method, but they are limited to 2D TMDCs with similar lattice structures and constants [19,20]. Recently, vdW heterostructures based on two distinct 2D materials with large lattice mismatch become increasingly attractive because their unique structures may result in some unusual physical properties [21,22]. However, unlike vdW heterostructures based on two 2D TMDCs, it is a significant challenge to directly grow this kind of vdW heterostructure due to the different numbers of atoms and bonding configurations within the two distinctively different 2D materials.

On the other hand, 2D layered halide perovskites have received much interests lately due to their superior physical properties, such as a high optical absorption coefficient, optimal bandgap, long carrier diffusion lengths, and good optical transport properties [23,24]. As a consequence, Chen and co-workers tried to prepare a kind of new heterostructure based on the 2D layered perovskite of $(C_4H_9NH_3)_2PbI_4$ with 200-nm-thickness and monolayer WS_2 by the exfoliation/transfer method and demonstrated a pronounced interlayer exciton emission [25]. $Cs_3Bi_2I_9$, as a member of 2D layered all-inorganic perovskite derivatives, has drawn considerable attention given the advantages of low-cost, earth-abundance, non-toxicity, and high-stability [26]. Herein, we developed a versatile two-step vapor phase route to achieve controlled growth of high-quality vertical vdW heterostructures based on 2D $Cs_3Bi_2I_9$ and $MoSe_2$, despite their large lattice mismatch. It is worth noting that not only the preparation method is totally different from previous literature on heterostructures based on the perovskites and TMDCs (**Table S1**), but the $Cs_3Bi_2I_9/MoSe_2$ vdW heterostructures also exhibit the advantages of being non-toxic and highly-stable [25,27–30]. Intriguingly, hybrid type-I and type-II band alignments were discovered in the $Cs_3Bi_2I_9/MoSe_2$ vdW heterostructure owing to the existence of defect energy level in $Cs_3Bi_2I_9$. More excitingly, the interlayer excitons from the type-II heterojunction exhibited a higher density and longer lifetime when compared with the previous vdW heterostructures made of exfoliated TMDCs. We attributed these properties to the reduced overlap of electron and hole wavefunctions caused by the large lattice mismatch. The direct growth of high-quality vdW heterostructures based on 2D TMDCs and perovskites with hybrid band alignments and long-lived interlayer excitons opens new venue toward exploring their novel physical properties for high-performance optoelectronics, valleytronics, and superfluidity.

Results and discussion

Fig. 1**a** shows the crystal structures of $Cs_3Bi_2I_9$ and $MoSe_2$ respectively, which reveals an obviously large lattice mismatch between the two kinds of 2D materials. Specifically, in $Cs_3Bi_2I_9$, each layer consists of 5 stacked atomic layers with a total thickness of ∼ 1.1 nm, packed in a hexagonal lattice with constants of a = b = 0.86 nm. While in $MoSe_2$, each layer has one atomic layer of Mo sandwiched between two identical Se layers (total thickness is ∼ 0.8 nm), packed in a hexagonal lattice as well, yet with different constants of a = b = 0.33 nm. The scheme for the growth of $Cs_3Bi_2I_9/MoSe_2$ heterostructures by the CVD method is shown in Fig. 1**b**. Briefly, $MoSe_2$ monolayers were grown on the SiO_2/Si wafer first by a controlled vapor deposition process [31]. The as-grown $MoSe_2$ monolayers were then used as templates for subsequent growth of $Cs_3Bi_2I_9$ few-layers to obtain the vertical vdW heterostructures. The growth temperature of the $MoSe_2$ template and the distance between the precursor and substrate need to be strictly controlled for this growth process [19]. More details about the sample synthesis can be found in the Methods section of supplementary material. This controllable, simple, and versatile growth method endows the $Cs_3Bi_2I_9/MoSe_2$ heterostructure a clean interface, the quality of which is superior to the samples obtained by manually stacking mechanical exfoliation 2D flakes [32,33]. Fig. 1**c-d** display optical microscopy (OM) images of $MoSe_2$ monolayer and $Cs_3Bi_2I_9/MoSe_2$ heterostructure, respectively. The lateral size of $MoSe_2$ monolayer is much larger than that of $Cs_3Bi_2I_9$, therefore $MoSe_2$ monolayer covers the entire image underneath the bright triangles (few-layer $Cs_3Bi_2I_9$) in the $Cs_3Bi_2I_9/MoSe_2$ heterostructure shown in Fig. 1**d**. The size of these triangles ranges from several to around 10 μm. The thicknesses of these few-layer $Cs_3Bi_2I_9$ were examined using atomic force microscopy (AFM) technique (**Fig. S1**). It was found that thicknesses of most of $Cs_3Bi_2I_9$ triangles are around 5.5 nm, which corresponds to 5-layer $Cs_3Bi_2I_9$. Raman spectroscopy was used to characterize the vertical $Cs_3Bi_2I_9/MoSe_2$ vdW heterostructure (Fig. 1**e**). Raman spectroscopy study of $Cs_3Bi_2I_9$ few-layer triangles on mica substrate was first performed as a reference, where the two Raman peaks at 109.1 and 146.0 cm^{-1} correspond to A_1^1 and A_1' modes of $Cs_3Bi_2I_9$ were clearly shown (the black curve in Fig. 1**e**) [26]. Raman spectra collected from the areas as indicated in blue dotted circle (Fig. 1**d**) only show the A_{1g} peak at 239.8 cm^{-1}, which confirms the bottom layer is the monolayer $MoSe_2$ (the blue curve in Fig. 1**e**) [34]. In the heterostructure region (areas marked by red dotted circle in Fig. 1**d**), three peaks at 108.5, 147.4, and 239.8 cm^{-1} were observed, which can be assigned to A_1^1 and A_1' modes of $Cs_3Bi_2I_9$ and A_{1g} mode of $MoSe_2$, respectively, confirming the formation of the vertical $Cs_3Bi_2I_9/MoSe_2$ vdW heterostructure. High-resolution Raman mapping images of a $Cs_3Bi_2I_9/MoSe_2$ vdW heterostructure were also collected, as shown in **Fig. S2**.
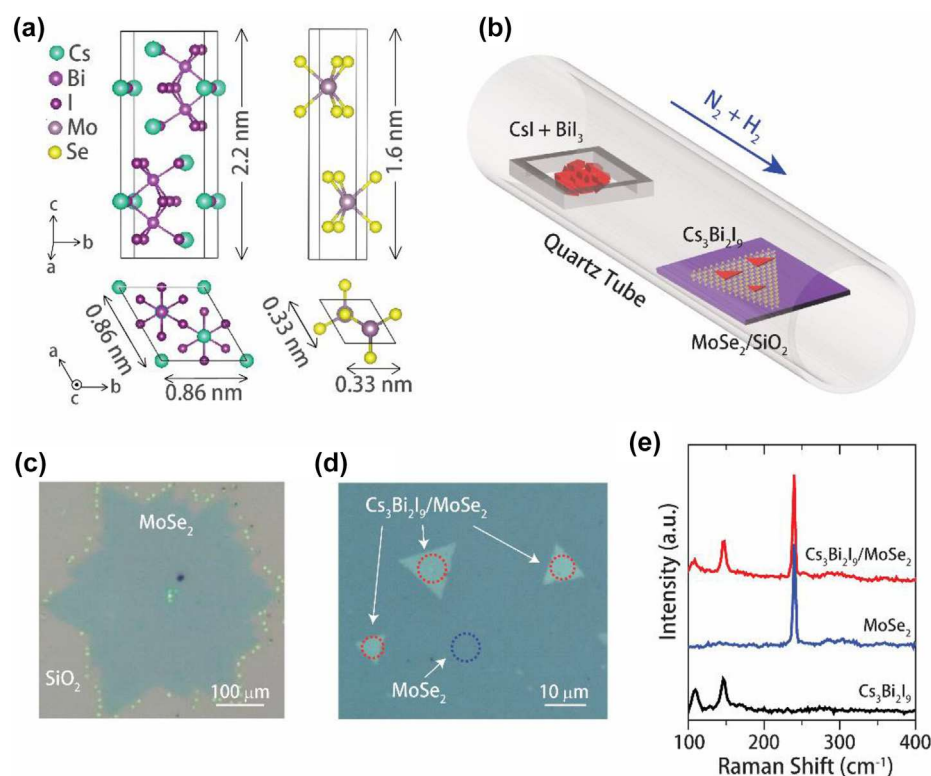
FIG. 1

Syntheses and structures of Cs$_3$Bi$_2$I$_9$/MoSe$_2$ vdW heterostructures. **a**, Crystal structures of Cs$_3$Bi$_2$I$_9$ and MoSe$_2$ from top and side views, respectively. For both materials, each unit cell contains two neighboring layers with a weak van der Waals interaction in between. The lattice constants of Cs$_3$Bi$_2$I$_9$ are a = b = 0.86 nm, c = 2.2 nm; while they are 0.33 nm and 1.6 nm for MoSe$_2$, respectively. **b**, Schematic of the growth process of Cs$_3$Bi$_2$I$_9$/MoSe$_2$ heterostructures by the CVD method. Step 1, the MoO$_3$ powder is used as the precursor to react with Se gas to grow MoSe$_2$ on the substrate of SiO$_2$/Si; Step 2, the mixture of CsI and BiI$_3$ is used as the precursor to grow Cs$_3$Bi$_2$I$_9$ on the substrate of MoSe$_2$/SiO$_2$/Si. Optical microscopy images of **c**, MoSe$_2$ and **d**, Cs$_3$Bi$_2$I$_9$/MoSe$_2$. MoSe$_2$ monolayer covers the entire image underneath bright triangles (few-layer Cs$_3$Bi$_2$I$_9$) in **d**. **e**, Raman spectra of an isolated Cs$_3$Bi$_2$I$_9$ flake (black curve), MoSe$_2$ monolayer (blue curve), and Cs$_3$Bi$_2$I$_9$/MoSe$_2$ heterostructure (red curve).

Fig. S2b–c shows the Raman mapping of peaks at 108.5, 147.4, and 239.8 cm^{-1}, respectively, further demonstrating the formation of the vertical Cs$_3$Bi$_2$I$_9$/MoSe$_2$ vdW heterostructure. Moreover, the Raman intensity distribution is uniform over the entire triangle, suggesting the high-quality of this heterostructure. This versatile approach can also be extended to the heterostructures based on Cs$_3$Bi$_2$I$_9$ and other TMDC materials by adjusting the growth factors. For instance, by changing the distance between the precursor and substrate, we also successfully prepared Cs$_3$Bi$_2$I$_9$/MoS$_2$ vdW heterostructure, as shown in **Fig. S3**.

The morphology of the Cs$_3$Bi$_2$I$_9$/MoSe$_2$ heterostructure was further examined by scanning electron microscopy (SEM). Fig. 2**a-b** show typical SEM images of this heterostructure, which exhibit well-defined triangle shapes of Cs$_3$Bi$_2$I$_9$ flakes, showing clear evidence of their high crystallinity. Because the size of MoSe$_2$ monolayer is much larger than that of Cs$_3$Bi$_2$I$_9$ (Fig. 1**d**), MoSe$_2$ monolayer covers the entire image in Fig. 2**a-b**. In order to better characterize this heterostructure, time-of-flight secondary ion mass spectrometry (ToF-SIMS) was applied to illustrate the 3D chemical information of this ultrathin heterostructure. Fig. 2**c** shows a typical 3D image of the Cs$_3$Bi$_2$I$_9$/MoSe$_2$ heterostructure, which exhibits two layers of the

heterostructure including the Cs$_3$Bi$_2$I$_9$ layer (the red triangle) and the MoSe$_2$ layer (the blue layer), as well as the substrate of SiO$_2$ (the green substrate). Chemical mappings of the three layers were plotted as well, as shown in Fig. S4**a**, which reveals that the chemical composition distributions in the Cs$_3$Bi$_2$I$_9$/MoSe$_2$ heterostructure are laterally uniform. Additionally, the chemical composition distributions in the Cs$_3$Bi$_2$I$_9$/MoSe$_2$ heterostructure are also vertically uniform, as shown in the ToF-SIMS depth profile in Fig. S4**b**. To further investigate the chemical compositions, X-ray photoelectron spectroscopy (XPS) was conducted on the Cs$_3$Bi$_2$I$_9$/MoSe$_2$ heterostructure. **Fig. S5** shows the survey spectrum of the Cs$_3$Bi$_2$I$_9$/MoSe$_2$ heterostructure, in which the elements of Cs, Bi, I, Mo, and Se were detected. After using the C1s peak at 284.6 eV to calibrate, the assignments of other peaks were determined. Fig. 2**d** shows the high-resolution XPS spectra of Cs 3d, Bi 4f, I 3d, Mo 3d and Se 3d regions. These binding energies are in good agreement with the intrinsic features of Cs$_3$Bi$_2$I$_9$ and MoSe$_2$ [26,35].

In order to reveal the band alignment and the interlayer interaction in the Cs$_3$Bi$_2$I$_9$/MoSe$_2$ vdW heterostructure, we investigated photoluminescence (PL) spectra of an isolated 5-layer Cs$_3$Bi$_2$I$_9$, an isolated monolayer MoSe$_2$, and a Cs$_3$Bi$_2$I$_9$/MoSe$_2$ vdW heterostructure with 532 nm excitation at 83 K respectively,
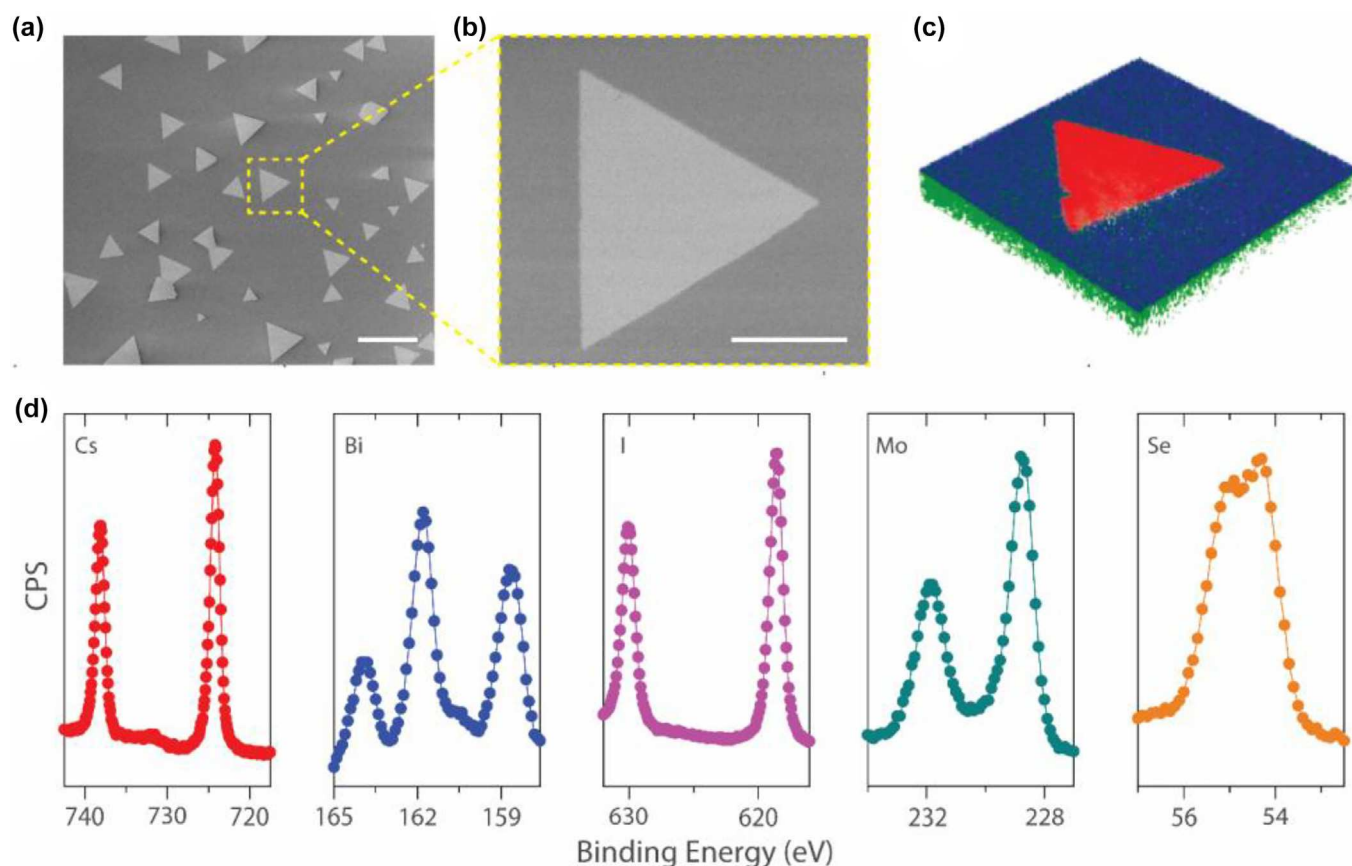
FIG. 2

Detailed characterizations of the $Cs_3Bi_2I_9$/MoSe$_2$ vdW heterostructures. **a-b**, SEM image of a $Cs_3Bi_2I_9$/MoSe$_2$ vdW heterostructure. The scale bars in **a** and **b** are 15 μm and 4 μm, respectively. **c**, 3D ToF-SIMS image of a $Cs_3Bi_2I_9$/MoSe$_2$ vdW heterostructure, including the $Cs_3Bi_2I_9$ layer (red triangle), the MoSe$_2$ layer (blue part) and the SiO$_2$ substrate layer (green part). **d**, High-resolution XPS spectra of a $Cs_3Bi_2I_9$/MoSe$_2$ vdW heterostructure, showing the existence of elements of Cs, Bi, I, Mo, and Se. According to the binding energies of five elements, the composition of this material can be indexed to $Cs_3Bi_2I_9$ and MoSe$_2$.

as shown in Fig. 3**a**. Clearly, 5-layer $Cs_3Bi_2I_9$ and monolayer MoSe$_2$ display strong PL peaks at 675 nm and 780 nm, respectively, which can be attributed to the excitonic transition energies in the two kinds of materials, and are in good agreement with previous reports [26,34,35]. A peak at 950 nm in monolayer MoSe$_2$ is attributed to the interface defects of MoSe$_2$. In the $Cs_3Bi_2I_9$/MoSe$_2$ vdW heterostructure, both PL peaks can be found easily, however, their intensities are significantly quenched, indicating efficient charge transfer in the heterojunction, reducing electron-hole recombination [36,37]. The two peaks are not quenched completely which may be ascribed to the relative high temperature of 83 K and a slightly large interlayer distance [38,39]. Meanwhile, the two PL peaks have slight shifts, which can be ascribed to the strong interlayer electronic coupling, further suggesting efficient charge transfer in this heterojunction [40,41]. What's more, another peak at 833 nm can be found in the PL spectra of this heterostructure. Unlike the peak at 950 nm, this peak cannot be ascribed to the defects in MoSe$_2$ generated during the second-step growth as the monolayer MoSe$_2$ before and after growing $Cs_3Bi_2I_9$ exhibit similar PL spectra, as shown in **Fig. S6**. Therefore, we speculated that this peak at 833 nm could be assigned to an interlayer exciton transition between the $Cs_3Bi_2I_9$ and MoSe$_2$ layers, indicating the $Cs_3Bi_2I_9$/

MoSe$_2$ vdW heterostructure possesses a type-II band alignment, similar to the commonly studied MoSe$_2$/WSe$_2$ vdW heterostructure [9]. In order to verify this speculation, we tested the temperature-dependent and laser power-dependent PL spectra of the $Cs_3Bi_2I_9$/MoSe$_2$ vdW heterostructure. Temperature-dependent PL spectra (**Fig. S7**) reveal an increase in the intensity of the 833 nm peak with decreasing temperature, consistent with interlayer exciton behavior seen in traditional TMDC/TMDC vdW heterostructures, which suggests the interlayer transitions in the $Cs_3Bi_2I_9$/MoSe$_2$ vdW heterostructure [10,15]. Fig. 3**b**, **Fig. S8**, and **Fig. S9** show the power-dependent PL spectra of the $Cs_3Bi_2I_9$/MoSe$_2$ vdW heterostructure. If the emission is from the interlayer excitons, the intensity of the peak will not saturate with increasing laser power. To confirm this point, we increased the laser power to 500 μW (**Fig. S8**), which is much higher than the saturation power commonly used in traditional TMDCs for defect-related emission [10,42]. The PL peak intensity (I) as a function of the laser power (P) was plotted, as shown in Fig. 3**c**. A fit by a power law ($I \propto P^\alpha$) to this curve yields α of around 0.87. Obviously, the PL intensity of the interlayer exciton increases sublinearly as the increasing laser power and no saturation trend appears in this curve even at much higher laser power, both of which suggest the observed emission at 833 nm in the
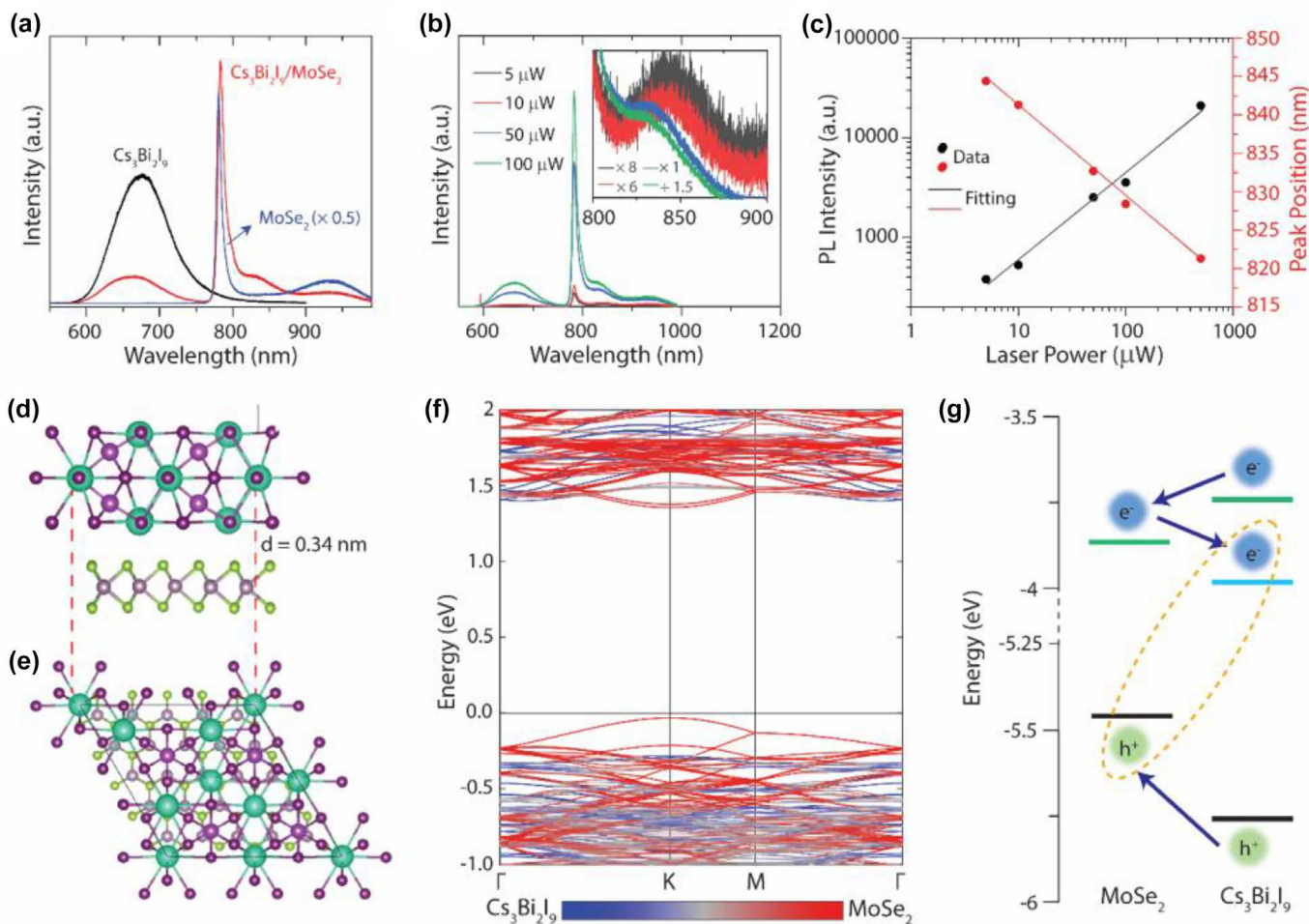
4

FIG. 3

Band alignments and interlayer excitons of Cs₃Bi₂I₉/MoSe₂ vdW heterostructures. **a**, Typical PL spectra of an isolated 5-layer Cs₃Bi₂I₉, an isolated monolayer MoSe₂, and a Cs₃Bi₂I₉/MoSe₂ vdW heterostructure with 532 nm excitation at 83 K. The isolated Cs₃Bi₂I₉ and MoSe₂ show strong PL at 675 nm and 780 nm, respectively. In the Cs₃Bi₂I₉/MoSe₂ vdW heterostructures, both exciton PL signals at 675 nm and 780 nm are strongly quenched, suggesting an efficient charge transfer process between the two components. Meanwhile, the shifts of the two peaks show strong interlayer coupling. Additionally, another peak at 833 nm appears, which is caused by interlayer excitons, indicating a type-II band alignment in the Cs₃Bi₂I₉/MoSe₂ vdW heterostructure. **b**, Power-dependent PL spectra of the Cs₃Bi₂I₉/MoSe₂ vdW heterostructure with 532 nm excitation at 83 K. Inset is the enlarged view of the range from 800 to 900 nm. In order to illustrate the peak position shifts, the intensities of the four curves were zoomed in or out manually. **c**, The PL intensity and peak position caused by interlayer excitons as a function of excitation laser power. The sublinear increase of PL intensity indicates the interlayer transitions in the Cs₃Bi₂I₉/MoSe₂ vdW heterostructure. The relatively large blue shift of peak position suggests a high interlayer exciton density. A supercell of the Cs₃Bi₂I₉/MoSe₂ vdW heterostructure viewed from **d**, side view and **e**, top view. **f**, Calculated band structure of the Cs₃Bi₂I₉/MoSe₂ vdW heterostructure, in which both CBM and VBM are located at the MoSe₂ layer, indicating a type-I band alignment in the pristine Cs₃Bi₂I₉/MoSe₂ vdW heterostructure. **g**, Schematic diagram of the band alignment of the Cs₃Bi₂I₉/MoSe₂ vdW heterostructure. In order to show the differences between CBM and the defect energy level (DEL) in the Cs₃Bi₂I₉ layer clearly, some parts between CBM and VBM are omitted. The CBM, VBM, and DEL are presented by green, black, and skyblue line, respectively.

Cs₃Bi₂I₉/MoSe₂ vdW heterostructure is indeed from interlayer exciton emission [14]. Additionally, Fig. 3**c** and the inset in Fig. 3**b** show that the PL peak of the interlayer exciton displays a blue shift with increasing laser power, which can be ascribed to the repulsive interaction between the dipole-aligned interlayer excitons. Moreover, the dipolar repulsion should result in an interlayer exciton density dependent blueshift of the emission energy with increasing the laser power [43]. This blueshift is up to around 40 meV, which is higher than that of the heterostructure based on two distinct TMDCs in the similar laser power range (10 meV), suggesting a higher interlayer exciton density in the Cs₃Bi₂I₉/MoSe₂ vdW heterostructure [15]. To quantify the interlayer exciton density, the exciton–exciton interaction

can be estimated via the mean-field approximation. This approximation uses the "plate capacitor formula": $E_{int} = 4\pi nde^2/\kappa$, where E_{int} is the exciton–exciton interaction energy, n is the exciton concentration, d is the separation between the layers, and κ is the dielectric constant [44]. Here, we assume the κ is in the same order of magnitude of 10 with Cs₃Bi₂I₉ and most of the TMDCs [45,46]. As a result, the interlayer exciton density of the Cs₃Bi₂I₉/MoSe₂ vdW heterostructure was calculated to be 0.52×10^{12} cm^{-2}, surpassing that of the reported MoSe₂/WSe₂ heterostructure[12] (supplemental material, **Note S1)**.

First-principles calculations were performed to understand the band alignment in the Cs₃Bi₂I₉/MoSe₂ vdW heterostructure, constructing a supercell with a 2 × 2 Cs₃Bi₂I₉ unit and 5 × 5 MoSe₂

unit to mitigate the lattice mismatch, as shown in Fig. 3**d-e**. This resulted in a biaxial strain of −4.9 % and 1.3 % on $Cs_3Bi_2I_9$ and $MoSe_2$, respectively. It is confirmed that this heterostructure is built up by vdW stacking of the $Cs_3Bi_2I_9$ layer and the $MoSe_2$ layer, and the distance between the two layers is around 0.34 nm. Fig. 3**f** presents that both conduction band minimum (CBM) and valence band maximum (VBM) of the heterostructure are attributed to $MoSe_2$ layer and located at the K point, indicating this heterostructure possesses a type-I band alignment, which is inconsistent with the result obtained from Fig. 3**a**. In order to comprehend this inconsistency, we measured the CBM and VBM of this heterostructure experimentally. The XPS valence band spectra of the isolated $Cs_3Bi_2I_9$ flake and the $Cs_3Bi_2I_9/MoSe_2$ heterostructure were shown in **Fig. S10**, from which the offset between two VBMs is 0.3 eV. Moreover, based on earlier reports from our group or others, the bandgaps of isolated $Cs_3Bi_2I_9$ and $MoSe_2$ have been determined to be 2.02 eV and 1.59 eV, respectively [26,34,35,47,48]. Therefore, the offset between two CBMs is 0.13 eV, as shown the type-I heterojunction in Fig. 3**g**. The type-II heterojunction observed in Fig. 3**a** is hypothesized to stem from defects within $Cs_3Bi_2I_9$, forming a defect energy level (DEL) between the CBM and VBM (Fig. 3**g**). These defects can be attributed the iodide vacancy (V_I) point defects based on previously calculated results [49]. In this type of band alignment, the electrons at the DEL of $Cs_3Bi_2I_9$ and the holes at the VBM of $MoSe_2$ form the interlayer excitons (Fig. 3**g**). Several observations support this hypothesis. First, as shown in Fig. 3**a**, the broader full width at half maxima (FWHM) of the $Cs_3Bi_2I_9$ peaks in both the isolated $Cs_3Bi_2I_9$ flake and the $Cs_3Bi_2I_9/MoSe_2$ heterostructure, compared to $MoSe_2$, suggest the existence of defect levels within the bandgap of $Cs_3Bi_2I_9$. Close observation reveals that the spectrum of the isolated $Cs_3Bi_2I_9$ flake is not symmetric and it can be divided into two peaks (**Fig. S11**), which originates from the intrinsic bandgap and defects of the $Cs_3Bi_2I_9$ flake, respectively. Second, we also performed the high-resolution transmission electron microscopy (HRTEM) of the $Cs_3Bi_2I_9$ flake, as shown in **Fig. S12**. Clearly, there are many defects in the $Cs_3Bi_2I_9$ flakes. Third, we tested the PL spectrum of the isolated $Cs_3Bi_2I_9$ flake at room temperature, as shown in **Fig. S13**, in which two main peaks at 615 nm and 695 nm can be found. The peak at 615 nm can be ascribed to the intrinsic bandgap of $Cs_3Bi_2I_9$, which is consistent with previous reports [50,51], while the peak locating at 695 nm can be ascribed to the defects. PL intensities of the two peaks are comparable, suggesting the defect density is very large and it is enough to form a DEL. The DEL locates 0.24 eV below the CBM of $Cs_3Bi_2I_9$, which is consistent with the peak position of interlayer exciton at 833 nm in Fig. 3**a**. Finally, it is well known that both electrons and holes locate at the same layer of the heterostructure and this layer will exhibit an enhanced PL intensity in a typical type-I heterostructure when compared with its individual sample. Therefore, the $MoSe_2$ layer should display an enhanced PL intensity in the $Cs_3Bi_2I_9/MoSe_2$ vdW heterostructure. However, Fig. 3**a** shows a decreased PL intensity of the $MoSe_2$ layer in the $Cs_3Bi_2I_9/MoSe_2$ vdW heterostructure. That is, another energy level extracts the electrons of the CBM of $MoSe_2$ quickly and hinders the formation of the intralayer excitons in the $MoSe_2$ layer when the electrons were transferred from $Cs_3Bi_2I_9$ to $MoSe_2$, further

indicating the existence of the DEL in between the bandgap of $Cs_3Bi_2I_9$. In conclusion, the $Cs_3Bi_2I_9/MoSe_2$ vdW heterostructure forms a type-I heterojunction, but exhibits properties akin to a type-II heterojunction due to the existence of the DEL within $Cs_3Bi_2I_9$'s bandgap.

The spatially separated nature of the interlayer exciton in a type-II heterojunction will lead to a reduced optical dipole moment, therefore its lifetime could be long. We investigated the lifetime of the interlayer exciton from the type-II heterojunction in the $Cs_3Bi_2I_9/MoSe_2$ vdW heterostructure by the time-resolved PL (TRPL) measurement. It is well known that radiative recombination of interlayer excitons is very hard to achieve at room temperature due to the dominating nonradiative recombination [52]. Therefore, all TRPL measurements were performed at cryogenic temperature. In this heterostructure, the lifetimes of intralayer excitons at 675 nm and 780 nm are substantially reduced by the ultrafast interlayer charge hopping (Fig. 3**a**) and they could be below the detection limits of the instrument. It is, therefore, very hard to obtain them in this study, even though we reduced the temperature to 10 K [36,37]. **Fig. S14** shows the temperature-dependent TRPL spectra of the interlayer exciton. The corresponding interlayer exciton lifetime was summarized in **Table S2**. Notably, the interlayer exciton lifetime becomes longer as the temperature decreases from 200 K to 10 K, which shows the same trend to interlayer exciton lifetime in literature [15,53]. The TRPL spectrum obtained at 200 K can be well fitted by a single-exponential decay function, while the TRPL spectrum obtained below 103 K can be analyzed by fitting to a biexponential decay function, from which two kinds of decay lifetime were obtained, including the fast decay lifetime of τ_1 and the slow decay lifetime of τ_2. Such behavior has been observed in TRPL curves of most materials, which can be explained by a three-level model, consisting of two closely spaced emitting states and a ground state, as shown in **Fig. S15** [54,55]. The fast decay lifetime of τ_1 is ascribed to interlayer exciton decay prior to thermalization between the lower and the upper emitting states. With the increase in temperature, the fast decay lifetime gradually disappears. In this case, the lifetime decay is represented by a single exponential, such as the TRPL spectrum obtained at 200 K. The slow decay lifetime of τ_2 can be attributed to the average of the interlayer exciton decays from the two emitting states to the ground state. The interlayer exciton lifetime is modeled by the Boltzmann factor of $\exp(-1/k_BT)$, as shown in **Fig. S15** [51–53]. Therefore, with the decrease in temperature, the slow decay lifetime increases dramatically. Fig. 4**a** shows the TRPL spectrum of the interlayer exciton at 833 nm at 83 K, which reveals the interlayer exciton lifetime $\tau_1 = 0.58$ ns and $\tau_2 = 3.67$ ns, which is longer than that of reported heterostructure under the same condition. Because the lifetime would show a drastic increase as decreasing temperature below 83 K, the TRPL measurement was conducted at 10 K as well [15]. Fig. 4**b** reveals that the interlayer exciton lifetime is prolonged to $\tau_1 = 14.23$ ns and $\tau_2 = 251.70$ ns at 10 K. Compared with traditional heterostructures based on 2D TMDCs, like $MoSe_2/WSe_2$ and $WSe_2/MoSe_2/WSe_2$, and novel heterostructures, like PbI_2/WSe_2, the interlayer lifetime of $Cs_3Bi_2I_9/MoSe_2$ vdW heterostructure is impressively long, indicating the promising potential of this new vdW heterostructure, as shown in Fig. 4**c** [9–16]. Optical transitions
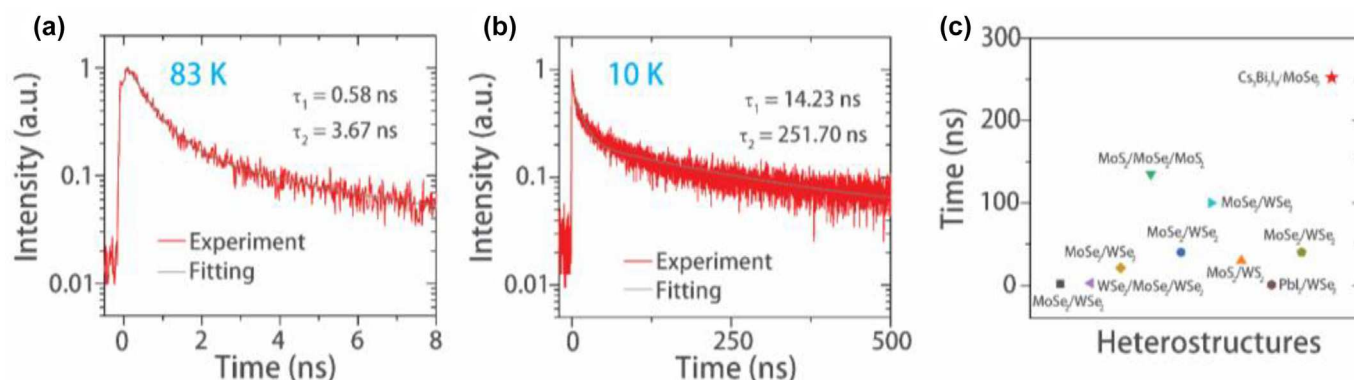
FIG. 4

Long-lived interlayer excitons of $Cs_3Bi_2I_9/MoSe_2$ vdW heterostructures. a, Time-resolved PL of the interlayer exciton at a, 83 K and b, 10 K. c, Comparison of the interlayer exciton lifetime of $Cs_3Bi_2I_9/MoSe_2$ vdW heterostructures with previously reported heterostructures. The lifetime of 1.8 ns for the $MoSe_2/WSe_2$ heterostructure from Ref. 9 was measured at 20 W, while the other heterostructures cited in the references were tested below 10 K.

involving the recombination of electrons and holes locating at different sites can only occur when there is an overlap between their corresponding orbitals, and the recombination will become harder as the overlap becomes smaller [56]. As mentioned above, the electrons and holes locate at the DEL of the $Cs_3Bi_2I_9$ layer and the VBM the $MoSe_2$ layer, respectively. In the $Cs_3Bi_2I_9/MoSe_2$ vdW heterostructure, due to the large lattice mismatch between $Cs_3Bi_2I_9$ and $MoSe_2$, this overlap will be smaller than traditional heterostructure based on two similar TMDCs. Therefore, the recombination of electrons and holes will become more difficult, resulting in a longer interlayer exciton lifetime. The long-lived interlayer excitons in vdW heterostructure have rich implications for valleytronic, optoelectronic, and superfluid applications. For instance, in scenarios where near-unity valley polarization is expected, the extended interlayer exciton lifetime in the $Cs_3Bi_2I_9/MoSe_2$ vdW heterostructure will require the generation of a prolonged valley lifetime, offering a favorable condition for information transfer in valley qubits. Moreover, the extraordinarily long lifetime has critical influence on exploring exotic physical phenomena, like Bose-Einstein condensation of excitons.

Conclusions

In summary, we reported a high-quality vertical $Cs_3Bi_2I_9/MoSe_2$ vdW heterostructure directly synthesized by a versatile two-step vapor phase route. Comparing with previous vdW heterostructure based on 2D TMDCs, the two atomically layered materials in this heterostructure have a large lattice mismatch. Intriguingly, hybrid band alignments, i.e. the co-existence of type-I and type-II heterojunctions, were demonstrated in the $Cs_3Bi_2I_9/MoSe_2$ vdW heterostructure for the first time. More importantly, different from previous reported type-II heterostructures, it is demonstrated that the type-II heterojunction in the $Cs_3Bi_2I_9/MoSe_2$ vdW heterostructure exhibits a higher interlayer exciton density and a longer interlayer exciton lifetime. We attributed these outstanding properties to the reduced electron and hole wavefunction overlap caused by the large lattice mismatch. Our study suggests that vdW heterostructures based on entirely different 2D materials, with high interlayer exciton density and long interlayer exciton lifetime, hold great promise for future studies of moire heterostructures, optoelectronics, valleytronics, and superfluidity.

CRediT authorship contribution statement

Jia Liang: Writing – review & editing, Writing – original draft, Methodology, Investigation, Formal analysis, Data curation. **Qing Ai:** Methodology, Formal analysis, Data curation. **Xiewen Wen:** Formal analysis, Data curation. **Xiuyu Tang:** Visualization, Investigation, Data curation. **Tianshu Zhai:** Investigation, Data curation. **Rui Xu:** Methodology, Data curation. **Xiang Zhang:** Investigation, Data curation. **Qiyi Fang:** Investigation, Data curation. **Christine Nguyen:** Investigation, Data curation. **Yifeng Liu:** Investigation, Data curation. **Hanyu Zhu:** Resources, Methodology, Investigation. **Tanguy Terlier:** Methodology, Data curation. **Gary P. Wiederrecht:** Resources, Methodology, Investigation. **Pulickel M. Ajayan:** Supervision, Resources. **Xiaofeng Qian:** Writing – review & editing, Supervision, Investigation, Formal analysis, Data curation. **Jun Lou:** Writing – review & editing, Writing – original draft, Supervision, Resources, Project administration, Investigation, Funding acquisition, Conceptualization.

Data availability

Data will be made available on request.

Declaration of competing interest

The authors declare that they have no known competing financial interests or personal relationships that could have appeared to influence the work reported in this paper.

Acknowledgements

RESEARCH: Original Research

Appendix A. Supplementary data

Supplementary data to this article can be found online at https://doi.org/10.1016/j.mattod.2024.02.008.

References

[1] J. Li et al., Nature 579 (2020) 368–374, https://doi.org/10.1038/s41586-020-2098-y.
[2] K. Choudhary et al., Phys. Rev. Mater. 7 (2023), 014009, https://doi.org/10.1103/PhysRevMaterials.7.014009.
[3] L.A. Jauregui et al., Science 366 (2019) 870–875, https://doi.org/10.1126/science.aaw4194.
[4] C.H. Jin et al., Nature 567 (2019) 76–80, https://doi.org/10.1038/s41586-019-0976-y.
[5] A. Castellanos-Gomez et al., Nat. Rev. Methods Primers 2 (2022) 58, https://doi.org/10.1038/nature12385.
[6] P. Rivera et al., Science 351 (2016) 688–691, https://doi.org/10.1126/science.aac7820.
[7] M.M. Fogler, L.V. Butov, K.S. Novoselov, Nat. Commun. 5 (2014) 4555, https://doi.org/10.1038/ncomms5555.
[8] P.V. Pham et al., Chem. Rev. 122 (2022) 6514–6613, https://doi.org/10.1021/acs.chemrev.1c00735.
[9] P. Rivera et al., Nat. Commun. 6 (2015) 6242, https://doi.org/10.1038/ncomms7242.
[10] B. Miller et al., Nano Lett. 17 (2017) 5229–5237, https://doi.org/10.1021/acs.nanolett.7b01304.
[11] C. Choi et al., Appl. 2 (2018) 30, https://doi.org/10.1038/s41699-018-0075-1.
[12] M. Troue et al., Phys. Rev. Lett. 131 (2023), 036902, https://doi.org/10.1103/PhysRevLett.131.036902.
[13] P. Nagler et al., x, Nat. Commun. 8 (2017) 1551, https://doi.org/10.1038/s41467-017-01748-1.
[14] M. Baranowski et al., Nano Lett. 17 (2017) 6360–6365, https://doi.org/10.1021/acs.nanolett.7b03184.
[15] P. Nagler et al., 2D Mater. 4 (2017), 025112, https://doi.org/10.1088/2053-1583/aa7352.
[16] C. Jin et al., Nat. Nanotech. 13 (2018) 994–1003, https://doi.org/10.1038/s41565-018-0298-5.
[17] P. Rivera et al., Nat. Nanotech. 13 (2018) 1004–1015, https://doi.org/10.1038/s41565-018-0193-0.
[18] Lin, Q. et al. A room-temperature moiré interlayer exciton laser. arXiv:2302.01266 (2023). https://doi.org/10.48550/arXiv.2302.01266.
[19] Y. Gong et al., Nat. Mater. 13 (2014) 1135–1142, https://doi.org/10.1038/nmat4091.
[20] Z. Cai et al., Chem. Rev. 118 (2018) 6091–6133, https://doi.org/10.1021/acs.chemrev.7b00536.
[21] B. Li et al., Adv. Electron. Mater. 2 (2016), 1600298, https://doi.org/10.1002/aelm.201600298.
[22] X. Li et al., Sci. Adv. 2 (2016), e1501882, https://doi.org/10.1126/sciadv.1501882.
[23] K. Leng et al., Nat. Mater. 17 (2018) 908–914, https://doi.org/10.1038/s41563-018-0164-8.
[24] L. Dou et al., Science 349 (2015) 1518–1521, https://doi.org/10.1126/science.aac7660.
[25] Y. Chen et al., ACS Nano 14 (2020) 10258–10264, https://doi.org/10.1021/acsnano.0c03624.
[26] J. Liang et al., Adv. Mater. 32 (2020), 2004111, https://doi.org/10.1002/adma.202004111.
[27] Q. Wang et al., ACS Nano 15 (2021) 10437–10443, https://doi.org/10.1021/acsnano.1c02782.
[28] H. Lai et al., Adv. Mater. 35 (2023), 2208664, https://doi.org/10.1002/adma.202208664.
[29] A. Elbanna et al., Opto-Electron Sci. 1 (2022), 220006, https://doi.org/10.29026/oes.2022.220006.
[30] J. Liang et al., Acc. Mater. Res. 3 (2022) 999–1010, https://doi.org/10.1021/accountsmr.2c00096.
[31] S. Najmaei et al., Nat. Mater. 12 (2013) 754–759, https://doi.org/10.1038/nmat3673.
[32] D.E. Purdie et al., Nat. Commun. 9 (2018) 5387, https://doi.org/10.1038/s41467-018-07558-3.
[33] M. Li et al., Mater. Today 19 (2016) 322–335, https://doi.org/10.1016/j.mattod.2015.11.003.
[34] S.-Y. Chen et al., Nano Lett. 15 (2015) 2526–2532, https://doi.org/10.1021/acs.nanolett.5b00092.
[35] Y. Yu et al., Nat. Chem. 10 (2018) 638–643, https://doi.org/10.1038/s41557-018-0035-6.
[36] H. Chen et al., Nat. Commun. 7 (2016), 12512, https://doi.org/10.1038/ncomms12512.
[37] H. Zhu et al., Nano Lett. 17 (2017) 3591–3598, https://doi.org/10.1021/acs.nanolett.7b00748.
[38] F. Liu et al., Phys. Rev. B 101 (2020), 201405(R), https://doi.org/10.1103/PhysRevB.101.201405.
[39] M. Van der Donck et al., Phys. Rev. B 98 (2018), 115104, https://doi.org/10.1103/PhysRevB.98.115104.
[40] A.F. Rigosi et al., Nano Lett. 15 (2015) 5033–5038, https://doi.org/10.1021/acs.nanolett.5b01055.
[41] X. Zhu et al., J. Am. Chem. Soc. 137 (2015) 8313–8320, https://doi.org/10.1021/jacs.5b03141.
[42] Z. Wu et al., Nano Res. 9 (2016) 3622–3631, https://doi.org/10.1007/s12274-016-1232-5.
[43] W. Li et al., Nat. Mater. 19 (2020) 624–629, https://doi.org/10.1038/s41563-020-0661-4.
[44] B. Laikhtman et al., Phys. Rev. B 80 (2009), 195313, https://doi.org/10.1103/PhysRevB.80.195313.
[45] N. Bu et al., J. Mater. Chem. C 10 (2022) 6665–6672, https://doi.org/10.1039/D2TC00599A.
[46] A. Laturia et al., npj 2D mater. Appl. 2 (2018) 6, https://doi.org/10.1038/s41699-018-0050-x.
[47] X. Wang et al., ACS Nano 8 (2014) 5125–5131, https://doi.org/10.1021/nn501175k.
[48] Y. Yang et al., Adv. Mater. 29 (2017), 1604201, https://doi.org/10.1002/adma.201604201.
[49] B. Ghosh et al., J. Phys. Chem. C 121 (2017) 17062–17067, https://doi.org/10.1021/acs.jpcc.7b03501.
[50] B.-W. Park et al., Adv. Mater. 27 (2015) 6806–6813, https://doi.org/10.1002/adma.201501978.
[51] F. Bai et al., Solar Energy Mater. Solar Cells 184 (2018) 15–21, https://doi.org/10.1016/j.solmat.2018.04.032.
[52] Y. Zhang et al., Adv. Mater. 31 (2019), 1901694, https://doi.org/10.1002/adma.201901694.
[53] Z. Li et al., ACS Nano 15 (2021) 1539–1547, https://doi.org/10.1021/acsnano.0c08981.
[54] X. Liu et al., 2D Mater. 3 (2016), 014001, https://doi.org/10.1088/2053-1583/3/1/014001.
[55] C. Donegá et al., Phys. Rev. B 74 (2006), 085320, https://doi.org/10.1103/PhysRevB.74.085320.
[56] J.S. Ross et al., Nano Lett. 17 (2017) 638–643, https://doi.org/10.1021/acs.nanolett.6b03398.